The modification of M41S materials: addition of metal clusters and nanoparticles†

Nicole S. Hondow,[a] George A. Koutsantonis,*[a] Rebecca O. Fuller,[ab] Hamzah Fansuri,[c] Martin Saunders,[d] Robert L. Stamps[b] and Dongke Zhang[c]

Received (in Victoria, Australia) 2nd November 2009, Accepted 22nd February 2010
First published as an Advance Article on the web 22nd April 2010
DOI: 10.1039/b9nj00626e

The incorporation of various molecular metal clusters, with well defined stoichiometry, into M41S materials has been investigated. The grafting of simple metal clusters, such as $[Ru_3(CO)_{12}]$ and $[PPN]_2[Fe_4(CO)_{13}]$, and the larger, and in one instance, bimetallic, clusters $[(dppe)_2Cu][Cu_6Fe_4(CO)_{16}]$ and $[PPh_4][Ru_{10}(\mu_6\text{-}C)(\mu\text{-}H)(CO)_{24}]$ has been achieved. Nanoparticles containing iron and platinum were also anchored on silaceous supports. The proportion of iron to platinum in FePt nanoparticles was adjusted by altering the molar ratios of starting materials. Consequently, ratios of Fe : Pt of 20 : 80, 27 : 73, 40 : 60, 53 : 47 and 64 : 36 were examined. The materials produced in this manner were characterised by Powder X-ray Diffraction (XRD), BET surface areas and Transmission Electron Microscopy (TEM) and elemental analysis. The FePt materials were also investigated for their magnetic properties by SQUID magnetometry. A number of the metal containing materials were investigated for their potential to produce hydrocarbons in the Fischer–Tropsch synthesis.

Introduction

Mesoporous silicas have excited chemists since the development of the M41S materials in 1992.[1,2] Their numerous desirable characteristics, such as large surface areas, well defined porous structure and a controllable narrow pore size distribution, make MCM-41 and MCM-48 attractive support materials. The silica M41S materials can after modification, often with transition metals, have potential uses in catalysis,[3] gas storage,[4] adsorption,[5] chromatography,[6] biomaterials,[7] chemical sensors[8] and optical/electronic devices.[9]

Our interest was in the use of these materials as supports for metal species for various applications including catalysis and magnetic media. It is salient to consider the ways developed to incorporate metal species in M41S materials and these can now be classified in two broad categories, namely, incorporation during the synthesis of the mesoporous silica and secondly by post-synthesis modification. In the first category, the most common incorporation methods are co-condensation and ion-exchange, which dope metals into the framework of the material, in the place of silicon atoms. While ion-exchange works by incorporating metals,[10] co-condensation can involve either the addition of metal sources[11] or siloxane and organo-siloxane precursors.[12,13] The latter is useful for organic functionalisation of the pore walls with potential ligands which can be later coordinated to metal species. It is also possible to modify the silicas with metals at this stage of synthesis through complexation,[14] where metal species which will form micelles with the template are used, and also through chemical vapour infiltration.[11]

These two approaches can be problematic.[15] The one-pot synthesis of the metal-modified M41S material holds obvious appeal as it is the simplest method for the incorporation of metals into the walls. In the case of catalyst development, embedding the metal in the framework can limit its contact with the reactants[11] and in these cases it is found that the properties of the silica predominate the effects of the dopant. A case in particular is aluminium ion-exchanged MCM-41, which does not exhibit similar acidity to the analogous zeolite materials attributed to the amorphous pore walls of the silicate.[13]

The three main post-synthesis modifications of the M41S materials methods are the wet impregnation of metal species, the functionalisation of the pore walls, and a series of reactions commonly termed 'grafting'. Wet impregnation is normally a very simple method involving the deposition of a metal, often in the form of a metal salt, onto the mesoporous silica,[10,11] and subsequent reduction. Functionalising the pore walls can be achieved in many ways, two of the most common involve either making the wall positively charged (hence allowing coordination of negatively charged metal species) or through the addition of silane coupling agents.[11] Grafting in the solution phase is far more common and this often involves the covalent bonding or anchoring of metal complexes with

[a] *Chemistry, M313, School of Biomedical, Biomolecular and Chemical Sciences, University of Western Australia, 35 Stirling Highway, Crawley, WA 6009, Australia. E-mail: george.koutsantonis@uwa.edu.au*
[b] *School of Physics, M013, University of Western Australia, 35 Stirling Highway, Crawley, WA 6009, Australia*
[c] *Centre for Petroleum, Fuels and Energy, University of Western Australia, 35 Stirling Highway, Crawley, WA, 6009, Australia*
[d] *Centre for Microscopy, Characterisation, and Analysis, M010, University of Western Australia, 35 Stirling Highway, Crawley, WA 6009, Australia*

† Electronic supplementary information (ESI) available: More detailed characterisation data and microscopy images of the materials. See DOI: 10.1039/b9nj00626e

their ligands reacting with the surface hydroxyl groups of the mesoporous silica.[10,11,16] The factors that need to be considered in the grafting of coordination or organometallic complexes have been considered in detail[17] and major issues exist over the retention of counterions, the size of aggregates produced when metal clusters are used, thermal stability and leaching of metal species. Despite these disadvantages it is possible to attempt to rationally design metal-containing species that can overcome the limitations previously found. Thus, oxophilic metals aid in the anchoring of the complex[18] and the use of charged anionic clusters hinder aggregation with coulombic forces acting and forming nanoparticulates. Organometallic metal clusters have the advantage of the easy incorporation of these properties and their synthesis is now a mature field. The use of metal clusters in the synthesis of nanoparticles and their incorporation into mesoporous silicas has also been explored.[16,18]

We are interested in the production of hydrocarbons *via* the Fischer–Tropsch process as applied to Gas-to-Liquids technology, *i.e.* the formation of hydrocarbons from synthesis gas derived from natural gas.[19,20] Metals known to be active for this process include iron, ruthenium, cobalt and nickel. Consequently, we have investigated the modification of the M41S materials with pre-formed, well-defined and characterised metal clusters and nanoparticles containing iron, ruthenium and platinum.

Experimental section

Preparation

The mesoporous silica materials were prepared *via* literature methods. Cubic MCM-48 was prepared[21] using a hydrothermal method, utilising tetraethylorthosilicate (TEOS) as a source of silicon and cetyltrimethylammoniumbromide (CTAB) as a structure directing agent. Briefly, the components of the mixture are added together such that a molar composition of 1 : 0.23 : 0.55 : 112 $SiO_2/Na_2O/CTAB/H_2O$ was obtained, and the resulting gel was crystallised under static hydrothermal conditions in a Teflon bottle for 3 days at 100 °C. Hexagonal MCM-41 was prepared[22] using a room pressure and temperature method, also utilising TEOS as a source of silicon and CTAB as a structure directing agent. Briefly, the components of the mixture are added together such that a molar composition of 1 : 1.64 : 0.15 : 126 $TEOS/NH_4OH/CTAB/H_2O$ was obtained, and the resulting gel was stirred overnight. In both cases, the powder was collected by filtration, and washed extensively with water and ethanol. The removal of the surfactant was achieved by overnight calcination in a furnace at 550 °C, with the first hour conducted under a flow of nitrogen.

The metal clusters, $[Ru_3(CO)_{12}]$,[23] $[PPh_4][Ru_{10}(\mu_6\text{-}C)(\mu\text{-}H)(CO)_{24}]$,[24] $[PPN]_2[Fe_4(CO)_{13}]$,[25] and $[(dppe)_2Cu][Cu_6Fe_4(CO)_{16}]$[26] and nanoparticles containing iron and platinum were prepared by literature procedures.[27,28] The proportion of iron to platinum in FePt nanoparticles was adjusted by altering the molar ratios of starting materials. Consequently, ratios of Fe : Pt of 20 : 80, 27 : 73, 40 : 60, 53 : 47 and 64 : 36 were examined, and these will furthermore be referred to as Fe_xPt_y, x and y referring to the percentage ratio of atoms.

In the reactions involving the addition of the metal clusters to the porous silicas, the metal clusters were initially dissolved in a solvent (for example, CH_2Cl_2 or THF) and added to a sample of dried M41S material. The resulting mixture was then either stirred or refluxed under argon, sometimes in the presence of NEt_3, for a period of time (between 1 and 7 days). After which, the solid was collected by filtration, the excess unreacted cluster removed *via* washing with the reaction solvent and the solid dried under vacuum. In the reactions involving the addition of the nanoparticles to the porous silica, a suspension of the purified nanoparticles suspended in hexane was added to a sample of dried M41S material. This was then stirred (90 min) after which the powder was collected *via* filtration, washed with hexane and dried under vacuum.

Calcinations of the metal modified M41S materials were conducted at temperatures between 250 and 550 °C, under atmospheres of nitrogen or air. In general, a small mass loss was associated with this calcination step.

Characterisation

Powder X-ray diffraction (XRD) was carried out using a Siemens D5000 diffractometer with Cu-Kα radiation generated at 40 kV and 35 mA. XRD scans employed a step size in 2θ of 0.03° and a step time of 15.0 s, over a range of 1.800° to 90.030° 2θ. Surface areas of samples were measured on a Micrometrics Tristar BET instrument at 77 K using nitrogen. Prior to analysis the sample was degassed for several hours at a pressure of 0.1 millibar and a temperature of 150 °C on a Micrometrics Vac Prep 061. Transmission Electron Microscopy (TEM) was performed on a JEOL 3000F FEG TEM at an operating voltage of 300 kV. The samples were prepared by dispersing a small amount of compound suspended in ether on a 200 mesh square holey carbon coated copper or gold grid (ProSciTech). Elemental analysis was conducted using an Oxford Instruments INCA 200 EDS system.

Magnetic measurements

All magnetic measurements were performed on a Quantum Design MPMS-7 SQUID magnetometer. Temperature-dependent magnetisation was measured using standard zero field cooled and field cooled techniques in a 100 Oe between 5 and 350 K. Hysteresis loops were also measured after being ZFC with fields up to 7 T at temperatures of 5 and 300 K.

Testing

Testing for the metal-modified M41S materials catalytic ability in the Fischer Tropsch process was conducted using a reactor through which a flow of H_2/CO could pass. A pre-mixed gas supply of 5.5% CO and 11.45% H_2 in N_2 was delivered through the reactor (either glass or stainless steel) at a rate of 24.1 mL min^{-1}. Gas samples were collected after passing through a bed of the catalyst (100 mg) and analysed using gas chromatography (Varian STAR 3400CX with FID detector). Retention times were compared to those of standard gases.

Results and discussion

Metal cluster incorporated M41S materials

The incorporation of various metal clusters into M41S materials has been investigated by us and others.[18,29,30] Considering our interest in the Fischer–Tropsch process we have focused on clusters containing the catalytically relevant elements iron and ruthenium. The grafting of simple metal clusters, such as $[Ru_3(CO)_{12}]$ and $[PPN]_2[Fe_4(CO)_{13}]$, and the larger, and in one instance, bimetallic, clusters $[(dppe)_2Cu][Cu_6Fe_4(CO)_{16}]$ and $[PPh_4][Ru_{10}(\mu_6\text{-}C)(\mu\text{-}H)(CO)_{24}]$ is the focus of the first part of this work. The interaction of anionic clusters with the MCM-41 surface is thought to occur between the Si–OH group of the surface and the OC–M group, and the intermolecular coulombic repulsion prevents aggregation of the metal particles during calcination.[18,31]

Ruthenium cluster attachment

While we sought to develop systems for the conversion of synthesis gas we thought it salient to consider the grafting of homometallic species but it soon became apparent that neutral $[Ru_3(CO)_{12}]$ would not adhere to the mesoporous material. Attempts had been made previously to form ruthenium impregnated silaceous materials using $[Ru_3(CO)_{12}]$ but it is unclear whether the cluster was in fact anchored to the surface.[32] Our problem was overcome by using the charged cluster, $[NHEt_3][Ru_3H(CO)_{11}]$,[33,34] which was formed by the *in situ* reaction of MCM-41 with $[Ru_3(CO)_{12}]$, triethylamine and water. This reaction resulted in the isolation of a grey powder, **Ru_3/MCM-41**, which was initially characterised by powder X-ray diffraction (XRD). The patterns of the resulting powder showed the retention of the three reflections assigned to the MCM-41 material ((100), (110) and (200)) and an additional broad reflection assigned to amorphous SiO_2 at 22° 2θ,[35] but nothing attributable to metal species was noted. Additionally, a large decrease in surface area of over 750 $m^2\ g^{-1}$ between the two materials was measured, indicating that the mesoporous silica had undergone changes, which had reduced the surface area of the material. Imaging of the material using bright field transmission electron microscopy, Fig. 1(a), immediately showed the presence of the highly ordered pore structure of the MCM-41. Upon further investigation with High Resolution TEM (HRTEM), what is believed to be small metal particles, *ca.* 1.7 nm in diameter, have been imaged, Fig. 1(b), showing that the metal complex has been included in the mesoporous silica. This was further confirmed using another technique, High Angle Annular Dark Field Scanning TEM (HAADF STEM), in which atomic number contrast has enabled the imaging of the heavier ruthenium particles on the lighter molecular weight silica (Fig. 1(c)). This useful technique made apparent the well dispersed nature of the particles. Elemental analysis of the material, using EDS, confirmed that the high-Z particles contained ruthenium. EDS spectra were obtained in STEM mode by scanning ~1 nm across a small region of the sample containing a high density of white particles.

Similar results were obtained when the higher nuclearity cluster $[PPh_4][Ru_{10}(\mu_6\text{-}C)(\mu\text{-}H)(CO)_{24}]$ was added to MCM-48.

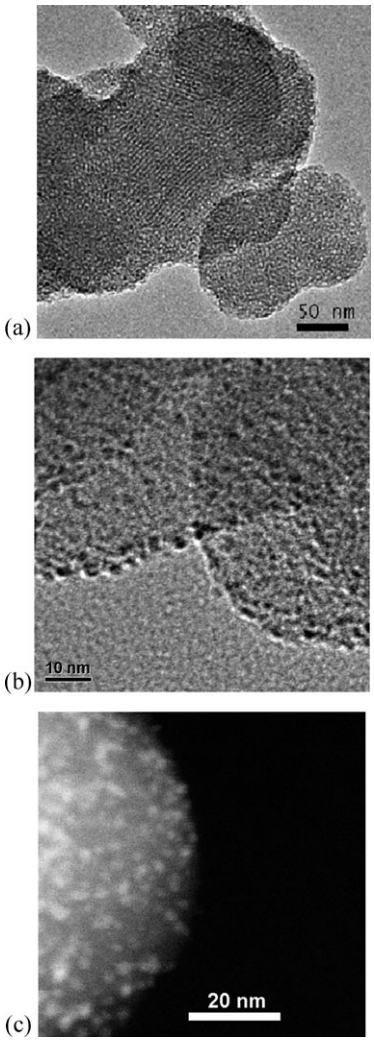

Fig. 1 TEM images of **Ru_3/MCM-41** showing the formation of ruthenium nanoparticles. (a) Low magnification, bright field, (b) high resolution, (c) HAADF STEM.

This afforded a pale grey powder, **Ru_{10}/MCM-48**, which yielded analogous data to the previous reaction, showing only XRD reflections due to the mesoporous MCM-48 ((211) and (220)), and a similar decrease in surface area (Δ650 $m^2\ g^{-1}$). The initial TEM images showed well ordered mesoporous silica, and EDS studies confirmed the presence of a low concentration of ruthenium. There did not appear to be many of these ruthenium particles and they were distributed through the material, however HRTEM and HAADF STEM imaging confirmed their presence (Fig. 2(b) and (c)). These particles were measured to be in the range of *ca.* 1.3 to 2.3 nm in diameter. Using HRTEM the planar spacings of the particle were determined, showing it to be the hexagonal ruthenium spacing (11 20) (2.056 Å).

The materials produced by the addition of the ruthenium clusters to the mesoporous silicas are quite similar, with comparable particle sizes produced from both of the clusters used. The material produced by the addition of $[Ru_3(CO)_{12}]$ has an average particle size of 1.7 nm, measured from 40 particles with a standard deviation of 0.44, while the $[PPh_4][Ru_{10}(\mu_6\text{-}C)(\mu\text{-}H)(CO)_{24}]$ incorporated material has an average particle size of 1.5 nm, measured from 76 particles

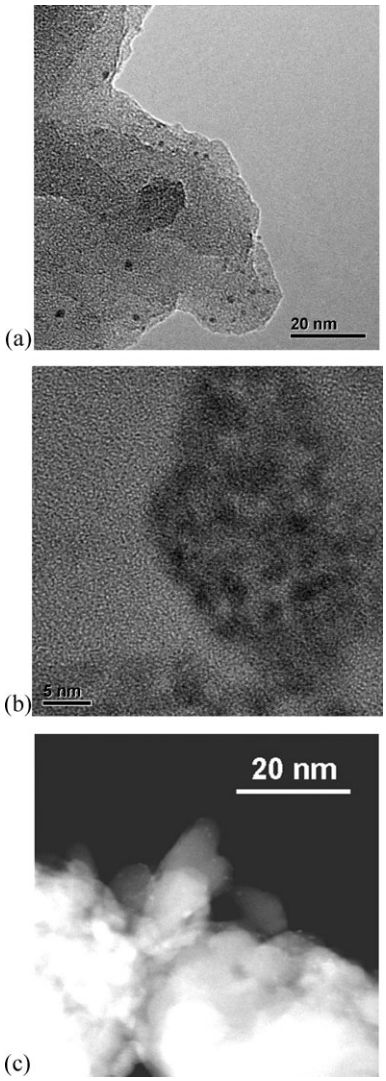

Fig. 2 TEM images of **Ru_{10}/MCM-48** showing the formation of ruthenium nanoparticles. (a) Low magnification, bright field, (b) high resolution, (c) HAADF STEM.

with a standard deviation of 0.50. However, the limitations of using TEM as an effective particle measurement tool for these materials is highlighted by the particles observed in Fig. 2(a). This section of the material made of MCM-48 with incorporated $[PPh_4][Ru_{10}(\mu_6\text{-}C)(\mu\text{-}H)(CO)_{24}]$, has an average particle size of 2.3 nm (13 particles, standard deviation 0.50), significantly larger than the overall average of 1.5 nm (obtained from several images taken from different parts of the material). The nature of the TEM allows only small areas to be analysed at any one time, and consequently account cannot be made for bulk characteristics. It is also found that images with more obvious particles, such as that in Fig. 2(a), can be obtained after the sample has been damaged by the electron beam as evidenced by loss of the regular structure afforded by the pores of the M41S material.

Calcination of the ruthenium grafted materials

A study of the conditions for optimal calcination of the materials was undertaken, Table 1. The requirement for calcination was based on the need to remove the supporting carbonyl ligands with the added requirement of retaining small particle size. The strength of the clusters attachment to the MCM material will dictate the size of the aggregates obtained. In the case of **Ru_3/MCM-41** the various conditions resulted in an increase in BET surface area of the calcined material, close to that of the unmodified MCM-41 (*ca.* 1000 $m^2\ g^{-1}$).

Table 1 Calcination conditions

T/°C	Time/h	Atmosphere	BET surface area/$m^2\ g^{-1}$
250	2.5	N_2	971
300	3	N_2	889
400	4	Air	918
550	15	Air	939

The measured XRD patterns of the calcined materials appear to vary with calcination temperature. The three higher calcination temperatures (300, 400 and 550 °C) all lead to diffraction patterns that contained not only reflections attributable to MCM-41, but also reflections assigned to tetragonal RuO_2. The lower calcination temperature (250 °C) resulted in a material whose XRD pattern had reflections attributed to MCM-41 (and that due to amorphous SiO_2). TEM imaging of the materials produced at the higher calcination temperatures shows extensive aggregation of the metal complex (Fig. 3). In all three materials there is no particle formed of consistent size, with imaged Ru particles, confirmed by EDS, ranging in size from 20 nm to as large as 300 nm in diameter.

The material calcined at 250 °C did not show evidence of aggregation as determined from the features observed in the XRD pattern or TEM images obtained. In the latter case, images of this material displayed only regularly arranged pores, and elemental analysis suggested the presence of ruthenium particles throughout and not in localised areas of aggregation. This suggests that the original ruthenium cluster species is not particularly well attached to the silica, and that it is quite mobile under relatively harsh calcination conditions.

Iron cluster attachment

The grafting of an iron cluster, $[PPN]_2[Fe_4(CO)_{13}]$, to MCM-41 produced similar results. The initial attachment reactions, conducted under various conditions all resulted in pink coloured materials, **Fe_4/MCM-41**. However, in these cases there appeared to be no evidence of crystalline iron clusters in the powder XRD pattern but a decrease in BET surface area compared to the unmodified MCM-41 was measured (Δ *ca.* 400 to 600 $m^2\ g^{-1}$, depending upon reaction conditions). In the case of the ruthenium complexes this often suggested that they had indeed been grafted onto the silaceous material and this was subsequently confirmed by EDS. TEM imaging confirmed that the regular porous structure of the MCM-41 was retained Fig. 4(a).

Calcination of the iron-containing materials at high temperatures (550 °C) did lead to a very small amount of aggregation of the cluster. The XRD patterns did not provide evidence of extensive aggregation but a number of larger crystallites were observed in the TEM images of this material, one of the largest observed is depicted in Fig. 4(b). EDS

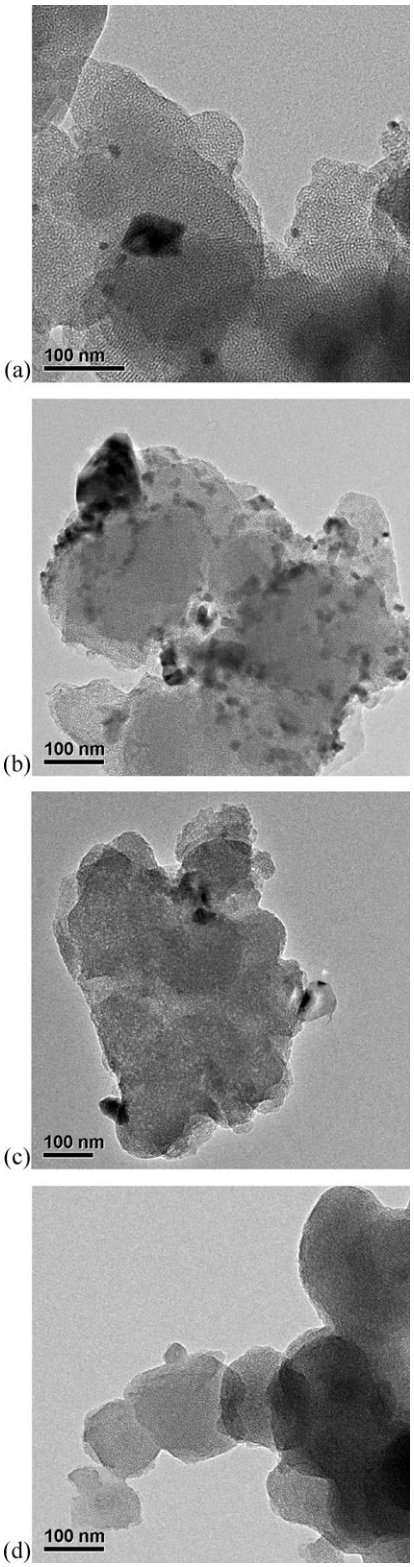

Fig. 3 TEM images of the calcined Ru_3/MCM-41 material at different calcination temperatures: (a) 550, (b) 400, (c) 300 and (d) 250 °C.

suggested the presence of iron particles throughout the material obviously reflecting a varied particle size distribution. As with the ruthenium-containing materials, calcination at lower

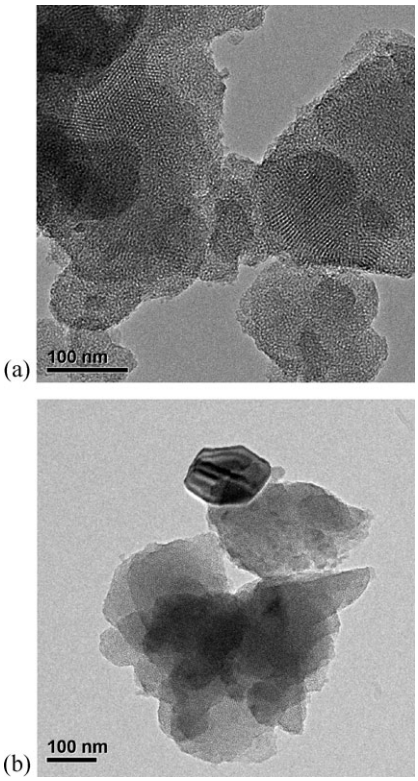

Fig. 4 TEM images of Fe_4/MCM-41: (a) after initial grafting, (b) after calcination at 550 °C.

temperatures (300 °C) caused no aggregation, as shown by XRD and TEM. All materials showed an increase in surface area, as the supporting ligands were removed.

Bimetallic cluster attachment

The grafting of the higher nuclearity, bimetallic cluster $[(dppe)_2Cu][Cu_6Fe_4(CO)_{16}]$ with the M41S materials was also investigated. Initial reaction of the cluster with MCM-48 in dichloromethane was unsuccessful, with little or no incorporation of the cluster into the silicate as judged by XRD and TEM/EDS, and only a small decrease in surface area was measured. Consequently, NEt_3 was added, in an attempt to activate the surface silanols of the MCM-48,[36] presumably by deprotonation. The materials activated in this way did appear to incorporate the cluster more successfully and EDS analysis suggested the incorporation of iron and copper throughout the silicate material accompanied by decreases in measured surface area: material denoted **FeCu/MCM-48**. Further, reflections observed in the XRD pattern were found in the region higher than 20° 2θ, which can be assigned to the (400) and (331) of cubic copper. We suspect that the complex cation in the grafting material has been reduced to Cu, while the triethylamine has been oxidised.[37–40] Further investigation by TEM, Fig. 5, does reveal some small copper crystals, as well as well-ordered porous silica materials also containing copper and iron. Calcination of the materials in moderate conditions (300–400 °C) did not lead to any observed aggregation of the Cu/Fe cluster. TEM and XRD measurements indicated that small amounts of CuO were formed and increases in surface

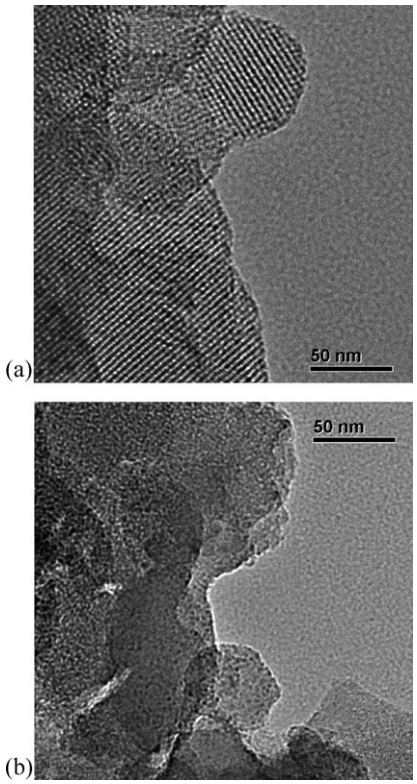

Fig. 5 TEM images of the grafting of FeCu/MCM-48: (a) as-synthesised MCM-48, (b) calcined at 400 °C.

area were measured, with values often in excess of 1000 $m^2\ g^{-1}$ (still short of the unmodified MCM-48 of 1375 $m^2\ g^{-1}$).

The materials resulting from the grafting of the iron cluster and the bimetallic copper/iron clusters appeared to be very similar. In both cases, while EDS confirmed the presence of the metals, it was difficult to accurately determine the size and location of the metal species by TEM or STEM imaging. As these techniques have been successfully applied to our other systems, this suggests that the particles are very small and, due to their lower atomic number, more difficult to observe within the silica matrix.

The four clusters that we have attempted to incorporate into M41S materials have all been incorporated to some extent. It is not possible to accurately determine the percentage incorporation by any of our available techniques. Our EDS studies, conducted using a Transmission Electron Microscope, were not quantitative, and attempts at quantitative EDS in SEM were unsuccessful due to the nature of the compounds. The silicate materials are not flat and this variation in topography makes it difficult to obtain accurate quantitative determination. Methods for the complete removal of the metal species from the silicate (by means of acid, base) were unsuccessful. What is clear is that not all of the cluster added during the synthesis was incorporated, as there was excess cluster collected after filtration and washing of the products.

Nanoparticle incorporated M41S materials

As part of on-going research we have investigated the synthesis of FePt nanoparticles for application to magnetic storage media[28] and we have recently published a short letter outlining the preliminary synthesis, characterisation and magnetic properties of these anchored on MCM-41.[41] Nanoparticles consisting of iron and platinum (FePt nanoparticles) have been the focus of considerable research recently, especially in the area of high density magnetic data storage.[42,43] One of the issues surrounding nanoparticles is their stability, they are prevented from aggregating by the addition of surfactants and other organic molecules. Incorporating these nanoparticles into M41S materials could remove the requirement for the surfactants, and even if their magnetic properties are not ideal[41] they are still prospective catalytic materials.

Access to the FePt nanoparticles was afforded by easily reproduced literature procedures and these nanoparticles were purified and characterised.[27,28] While a range of FePt compositions could be obtained we investigated in detail the ratios 27 : 73 and 20 : 80 and the materials obtained from both are similar. The addition of a hexane suspension of the $Fe_{27}Pt_{73}$ nanoparticles to a suspension of MCM-41, in hexane, resulted in the complete grafting of the nanoparticles. The resulting powder, **$Fe_{27}Pt_{73}$/MCM-41**, was collected by filtration and characterised, the solvent was now colourless unlike the surfactant stabilised solution/suspension of FePt nanoparticles which was previously black. The powder XRD pattern of **$Fe_{27}Pt_{73}$/MCM-41** contained only reflections assignable to the supporting MCM-41 material ((100), (110) and (200)) and in some samples, the broad reflection assigned to amorphous SiO_2. No reflections due to the FePt nanoparticles were observed, presumably due to their small size and relative concentration (compared to that of the MCM-41), similar to the examples where the metal clusters were incorporated. The BET surface area measurements all showed a decrease in surface area after the incorporation of the nanoparticles. The decrease in surface area was generally between 150 and 350 $m^2\ g^{-1}$, from an original, unmodified surface area of 1000 $m^2\ g^{-1}$.

TEM has been far more useful in characterising these materials. Bright field imaging has again shown that the MCM-41 has retained its porous nature and the small FePt nanoparticles are also visible (Fig. 6(a) and (b)). The utility of adding well characterised nanoparticles to the porous support is that the size and size distribution prior to their grafting to MCM-41 is known. These features were confirmed by HRTEM (Fig. 6(c)) from which it can be seen that the nanoparticles retain their original size and crystallinity. The crystallinity is confirmed by a Fast Fourier Transform (FFT) power spectrum (inset Fig. 6(c)) of one of the particles showing a pattern that is assigned to the (111) plane of FePt alloy ($\sim$0.22 nm). These images show a material with $Fe_{27}Pt_{73}$ nanoparticles, of *ca.* 4 nm in size, with the fcc ordering of the particles imaged (Fig. 6(c)). There is no evidence from TEM that aggregation of the particles has occurred, in fact imaging suggests that the particles are well-distributed across an MCM-41 particle. This is emphasised by HAADF STEM imaging,[41]when imaging in this mode it is possible to view both the pores of the silicate and the well-dispersed nature of the FePt nanoparticles (Fig. 6(d)). While it is not possible to confidently determine whether the particles are present exclusively in the pores or on the surface with these techniques,

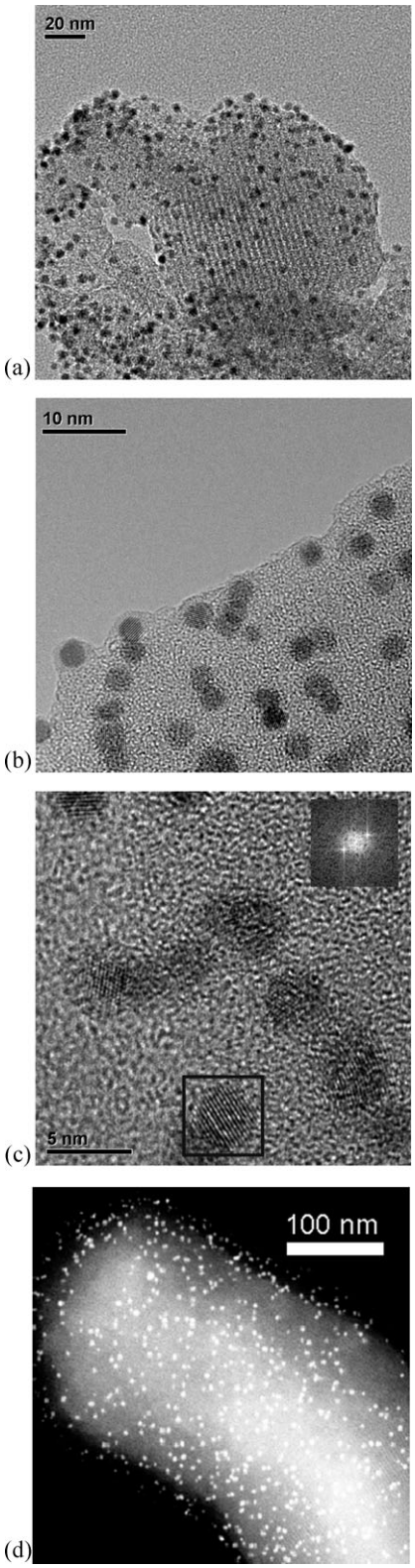

Fig. 6 (a) and (b) TEM, (c) HRTEM with inset showing FFT of the selected particle and (d) HAADF STEM images of one sample of **$Fe_{27}Pt_{73}$/MCM-41**.

it is expected that due to the FePt nanoparticles being larger than the pores of the MCM-41, a majority of the particles would be present on the surface.

The range of materials with varying FePt compositions were calcined to remove the surfactants and organic molecules that are no longer required to stabilise the FePt nanoparticles. Calcinations were conducted under a variety of conditions (200 to 560 °C), and evidence of aggregation was never found (by XRD or TEM). Surface areas increased to give materials with surface areas between 775 and 1000 $m^2\ g^{-1}$.

The advantages of this method of incorporation were emphasised when compared to other materials prepared by different methods. We investigated the synthesis of FePt grafted materials using a further three methods of incorporation of the FePt nanoparticles. The first involved the desolvation of a sample of suspended $Fe_{20}Pt_{80}$ nanoparticles and adding that dried sample to a sample of MCM-41. The TEM images obtained (Fig. 7(a)), suggests that this "solid-state" style reaction resulted in only a fraction of the nanoparticles being grafted into the silicate, with the remainder found apart from the MCM-41 support.

The second synthesis involved the addition of a sample of the $Fe_{20}Pt_{80}$ nanoparticles to the mixture from which MCM-41 is prepared and in this case there was no evidence that any nanoparticles had been incorporated. Thirdly, the high temperature synthesis of the nanoparticles was conducted in the presence of a sample of MCM-41 and from which TEM imaging suggested the presence of nanoparticles (Fig. 7(b)). Inspection of the image suggested that a relatively large size distribution was obtained, something we were attempting to avoid, and we propose[41] that this may provide a route to the synthesis of small (less than 2 nm) $Fe_{20}Pt_{80}$ nanoparticles.

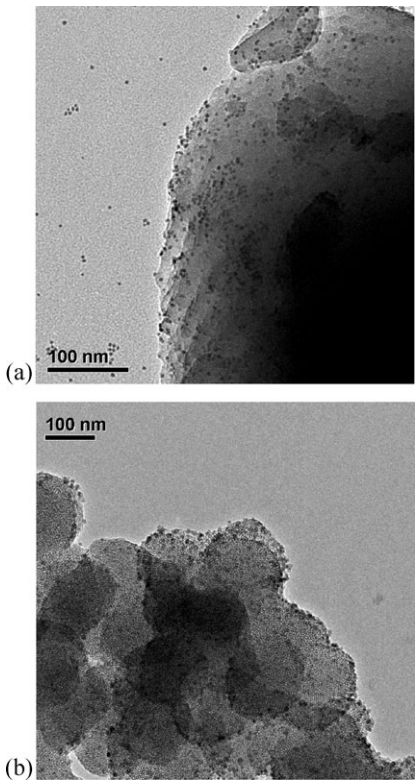

Fig. 7 TEM images of $Fe_{20}Pt_{80}$/MCM-41 (a) "solid-state" synthesis. (b) Material obtained from high temperature synthesis of FePt NPs in the presence of MCM-41.

These alternatives suggest that our relatively simple route involving the addition of a suspension of nanoparticles leads to materials with a small size distribution of particles and with no aggregation.

Magnetic measurements

Previous magnetic measurements[41] of the unannealed FePt particles incorporated into MCM silicates displayed magnetic properties similar to those of the as-synthesised particles. Regardless of composition, as-synthesised FePt particles exist in an unordered face centered cubic phase. Annealing of the particles leads to a change in the crystal structure and thus the magnetic properties.[44,45]

Annealing of $Fe_{20}Pt_{80}$ particles should lead to the formation of a Cu_3Au type phase with a $L1_2$ structure.[45] The choice of annealing temperature and time is critical to the results obtained,[44] thus a range of temperatures and annealing times were investigated. Results for when the sample was annealed at 500 °C in N_2 for 1.5 h and at 560 °C in N_2 for 1 h are presented.

After annealing, the FePt MCM samples magnetic properties change significantly. Fig. 8 shows the zero field cooled (ZFC) and field cooled (FC) magnetisation as a function of temperature for the sample when it is annealed to (a) 500 °C and (c) 560 °C. We do not see in Fig. 8(a) evidence for superparamagnetic behaviour of the unannealed system seen previously,[41] the system annealed at 500 °C is paramagnetic. This is further emphasized by the 5 K hysteresis loop shown in Fig. 8(b). The coercive field is zero consistent with a superparamagnet, that is behaviour above the blocking temperature. Hysteresis loops at 300 K were also performed that showed a dominant diamagnetic contribution from the silicate.

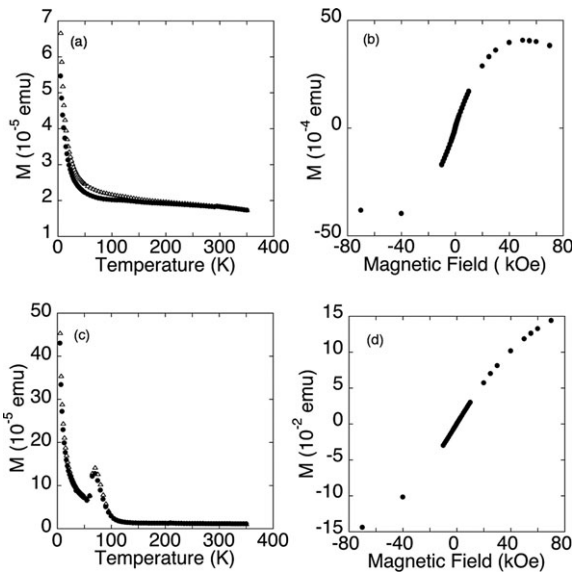

Fig. 8 Magnetisation as a function of temperature and field for $Fe_{20}Pt_{80}$ /MCM-41. Results after annealing are shown in (a) for 500 °C and (c) for 560 °C. ZFC data is shown as solid circles and open triangles are used for FC points. 5 K ZFC hysteresis loops of $Fe_{20}Pt_{80}$ /MCM-41 are shown, when annealed to 500 °C in (b) and 560 °C in (d).

When FePt–MCM was annealed at 560 °C the ZFC-FC magnetisation curves shown in Fig. 8(c) indicate the development of a magnetic phase between 50 and 100 K. The $FePt_3$ (Cu_3Au type phase) structure is magnetically ordered and it should be antiferromagnetic with T_N of less that 160 K.[46] We identify the peak at ~70 K as possibly indicating the onset of this ordering (Fig. 8(c)). It suggests a significant component of blocked magnetic moments with a blocking temperature of ~70 K. The 300 K hysteresis loop again was dominated by the diamagnetic contribution of the silicates. At 5 K the system does not saturate at high applied fields and Hc is zero. This is consistent with antiferromagnetic ordering.

Annealing of Pt-rich alloys leads to the outer most (111) layer containing Pt exclusively with the subsequent second and third layers of Fe binary alloys decreasing monotonously in Pt concentration.[47,48] The ordering of the FePt particles cannot be confirmed through XRD due to the low concentration of particles compared to that of the silicate. However, the development of an antiferromagnetic phase suggests that platinum segregation in the lattice occurs, a phase found in ordered cubic $L1_2$ $FePt_3$. Previously[41] we postulated that the FePt particles adhere to the silicate surface through coulombic interactions as no metal–O–Si bonds were evident in the FTIR spectra of the unannealed sample. In addition, the particles could be partially removed through sonication in a high ionic strength solution. On annealing of the samples no agglomeration occurred. The only change to the FTIR spectra reported earlier[41] was the loss of the N–H stretch at 1551 cm^{-1} and C–H stretch at 2927 and 2856 cm^{-1} a result not unexpected after annealing, and related to the loss of surfactant. The migration of Pt to the surface would rule out FePt adhering to MCM-41 through Fe–O–Si interaction. The lack of any evidence for Pt–O–Si stretching after annealing supports the postulated coulombic interaction binding.

Preliminary catalyst testing

Preliminary catalyst testing for the Fischer–Tropsch process in a primarily qualitative manner has been undertaken. A mix of CO and H_2 in N_2 (5.5 CO : 11.45 H_2 : 83.05 N_2) was used as the feed synthesis gas, with products analysed by GC. Representative samples of the materials were tested, and in all cases, under a range of conditions, the major product formed was methane. Obviously, this was undesirable but the analysis then focused on identifying the minor products produced.

Testing of **Ru_3/MCM-41** gave a number of products that implied the production of C2 hydrocarbons (ethane, ethylene) and pentane, and with trace amounts of C3 (propylene), C4 (isobutane, 1-butene) and pentane. The iron-containing materials produced similar products, although in different ratios, and under different conditions, and also had trace amounts of hexane formed. The copper–iron containing material also produced a range of products from C2 to C6, though often only in trace amounts.

A range of the FePt nanoparticle incorporated materials were tested, including compounds that contained the ratios 20 : 80, 27 : 73, 40 : 60 and 47 : 53 of Fe : Pt. All compounds again produced C2 (ethane, ethylene) and C3 (propane,

propylene) hydrocarbons. It was found that the compounds with lower Fe% produced a wider range of products (up to C5 hydrocarbons) whereas those with higher Fe% produced less products (up to trace amounts of C4 hydrocarbons). Though this cannot be attributed entirely to the metal ratio, as the concentration of nanoparticles across the silicate may vary dramatically between materials.

Conclusions

We have prepared a series of metal-modified M41S materials which show some activity towards the Fischer–Tropsch process. The incorporation of the metal was achieved using two different types of metal species, both of which were synthesised separately to the silica material and were of a well-defined nature and fully characterised prior to addition. In the case of the metal clusters, incorporation was only achieved when charged clusters were used, and appropriate conditions had to be found to ensure that aggregation did not occur during calcination. Meanwhile, the addition of the FePt nanoparticles produced materials that contained metal species of a known size, that under all calcination conditions attempted did not aggregate. These materials showed some activity towards the Fischer–Tropsch process which could be further investigated, as could their activity towards other catalytic processes.

Acknowledgements

We thank the ARC Large Grant Scheme for funding this research. NSH and ROF were holders of Australian Post-graduate Awards. RLS and ROF thank Seagate Technologies for partial funding of this work. The authors acknowledge the facilities, scientific and technical assistance of the Australian Microscopy & Microanalysis Research Facility at the Centre for Microscopy, Characterisation & Analysis, The University of Western Australia, a facility funded by The University, State and Commonwealth Governments.

References

1 C. T. Kresge, M. E. Leonowicz, W. J. Roth, J. C. Vartuli and J. S. Beck, *Nature*, 1992, **359**, 710–712.
2 J. S. Beck, J. C. Vartuli, W. J. Roth, M. E. Leonowicz, C. T. Kresge, K. D. Schmitt, C. T.-W. Chu, D. H. Olson, E. W. Sheppard, S. B. McCullen, J. B. Higgins and J. L. Schlenker, *J. Am. Chem. Soc.*, 1992, **114**, 10834–10843.
3 A. Taguchi and F. Schüth, *Microporous Mesoporous Mater.*, 2005, **77**, 1–45.
4 V. C. Menon and S. Komarneni, *J. Porous Mater.*, 1998, **5**, 43–58.
5 A. Sayari, S. Hamoudi and Y. Yang, *Chem. Mater.*, 2005, **17**, 212–216.
6 V. Rebbin, R. Schmidt and M. Fröba, *Angew. Chem., Int. Ed.*, 2006, **45**, 5210–5214.
7 M. Vallet-Regí, *Chem.–Eur. J.*, 2006, **12**, 5934–5943.
8 B. Yuliarto, I. Honma, Y. Katsumura and H. Zhou, *Sens. Actuators, B*, 2006, **114**, 109–119.
9 B. Julián, J. Planelles, E. Cordoncillo, P. Escribano, P. Aschehoug, C. Sanchez, B. Viana and F. Pellé, *J. Mater. Chem.*, 2006, **16**, 4612–4618.
10 K. Moller and T. Bein, *Chem. Mater.*, 1998, **10**, 2950–2963.
11 J.-L. Shi, Z.-L. Hua and L.-X. Zhang, *J. Mater. Chem.*, 2004, **14**, 795–806.
12 F. Hoffmann, M. Cornelius, J. Morell and M. Fröba, *Angew. Chem., Int. Ed.*, 2006, **45**, 3216–3251.
13 B. Lindlar, M. Luchinger, A. Rothlisberger, M. Haouas, G. Pirngruber, A. Kogelbauer and R. Prins, *J. Mater. Chem.*, 2002, **12**, 528–533.
14 A. Pöppl, P. Baglioni and L. Kevan, *J. Phys. Chem.*, 1995, **99**, 14156–14160.
15 A. B. Bourlinos, A. Simopoulos, N. Boukos and D. Petridis, *J. Phys. Chem. B*, 2001, **105**, 7432–7437.
16 B. C. Gates, *Chem. Rev.*, 1995, **95**, 511–522.
17 J. Guzman and B. C. Gates, *Dalton Trans.*, 2003, 3303–3318.
18 S. T. Bromley, G. Sankar, C. R. A. Catalow, J. M. Thomas and T. Maschmeyer, *Microporous Mesoporous Mater.*, 2001, **44–45**, 395–399.
19 B. H. Davis, *Top. Catal.*, 2005, **32**, 143–168.
20 H. Schulz, *Appl. Catal., A*, 1999, **186**, 3–12.
21 J. Xu, Z. Luan, H. He, W. Zhou and L. Kevan, *Chem. Mater.*, 1998, **10**, 3690–3698.
22 D. Kumar, K. Schumacher, C. du Fresne von Hohenesche, M. Grun and K. K. Unger, *Colloids Surf., A*, 2001, **187–188**, 109–116.
23 M. I. Bruce, B. K. Nicholson and M. L. Williams, *Inorg. Synth.*, 1990, **28**, 221–230.
24 M. P. Cifuentes and M. G. Humphrey, *Inorg. Synth.*, 1998, **32**, 287–293.
25 K. H. Whitmire, J. Ross, C. B. Cooper, III and D. F. Shriver, *Inorg. Synth.*, 1982, **21**, 66–69.
26 G. Doyle, K. A. Eriksen and D. Van Engen, *J. Am. Chem. Soc.*, 1985, **107**, 7914–7920.
27 S. Sun, C. B. Murray, D. Weller, L. Folks and A. Moser, *Science*, 2000, **287**, 1989–1992.
28 R. O. Fuller, G. A. Koutsantonis, R. L. Stamps and F. Bardou, *J. Appl. Phys.*, 2005, **97**, 10J508-1–510J508-3.
29 W. Zhou, J. M. Thomas, D. S. Shephard, B. F. G. Johnson, D. Ozkaya, T. Maschmeyer, R. G. Bell and Q. Ge, *Science*, 1998, **280**, 705–708.
30 F. Schweyer, P. Braunstein, C. Estournes, J. Guille, H. Kessler, J.-L. Paillaud and J. Rose, *Chem. Commun.*, 2000, 1271–1272.
31 S. T. Bromley, G. Sankar, C. R. A. Catalow, T. Maschmeyer, B. F. G. Johnson and J. M. Thomas, *Chem. Phys. Lett.*, 2001, **340**, 524–530.
32 M. Hartmann, C. Bischof, Z. Luan and L. Kevan, *Microporous Mesoporous Mater.*, 2001, **44–45**, 385–394.
33 J. B. Keister, J. R. Shapley and D. A. Strickland, *Inorg. Synth.*, 1990, **27**, 196–208.
34 D. F. Shriver and D. W. Bruce, *Iron, Ruthenium and Osmium*, Permagon, New York, 1995.
35 L. Zhang, G. C. Papaefthymiou and J. Y. Ying, *J. Phys. Chem. B*, 2001, **105**, 7414–7423.
36 T. Maschmeyer, F. Rey, G. Sankar and J. M. Thomas, *Nature*, 1995, **378**, 159–162.
37 J. F. Weiss, G. Tollin and J. T. Yoke, III, *Inorg. Chem.*, 1964, **3**, 1344–1348.
38 J. T. Yoke, III, J. F. Weiss and G. Tollin, *Inorg. Chem.*, 1963, **2**, 1210–1216.
39 A. Adenier, M. M. Chehimi, I. Gallardo, J. Pinson and N. Vila, *Langmuir*, 2004, **20**, 8243–8253.
40 R. S. Davidson and K. R. Tretheway, *J. Chem. Soc., Perkin Trans. 2*, 1977, 173–178.
41 R. O. Fuller, N. S. Hondow, G. A. Koutsantonis, M. Saunders and R. L. Stamps, *J. Phys. Chem. C*, 2008, **112**, 5271–5274.
42 R. F. C. Farrow, D. Weller, R. F. Marks, M. F. Toney, A. Cebollada and G. R. Harp, *J. Appl. Phys.*, 1996, **79**, 5967–5969.
43 A. Cebollada, D. Weller, J. Sticht, G. R. Harp, R. F. C. Farrow, R. F. Marks, R. Savoy and J. C. Scott, *Phys. Rev. B: Condens. Matter*, 1994, **50**, 3419–3422.
44 S. Sun, E. E. Fullerton, D. Weller and C. B. Murray, *IEEE Trans. Magn.*, 2001, **37**, 1239–1243.
45 C.-B. Rong, Y. Li and J. P. Liu, *J. Appl. Phys.*, 2007, **101**, 09K505-501–509K505-503.
46 G. E. Bacon and J. Crangle, *Proc. R. Soc. London, Ser. A*, 1963, **272**, 387–405.
47 P. Beccat, Y. Gauthier, R. Baudoing-Savois and J. C. Bertolini, *Surf. Sci.*, 1990, **238**, 105–118.
48 C. Creemers and P. Deurinck, *Surf. Interface Anal.*, 1997, **25**, 177–190.

